ACS Energy LETTERS

http://pubs.acs.org/journal/aelccp

Defect-Tolerant TiO_2-Coated and Discretized Photoanodes for >600 h of Stable Photoelectrochemical Water Oxidation

Xin Shen, Maoqing Yao, Ke Sun, Tianshuo Zhao, Yulian He, Chun-Yung Chi, Chongwu Zhou, Paul Daniel Dapkus, Nathan S. Lewis,* and Shu Hu*

Cite This: *ACS Energy Lett.* 2021, 6, 193−200

Read Online

ACCESS | Metrics & More | Article Recommendations | Supporting Information

ABSTRACT: Arrays of GaAs nanowires have been grown by selective-area metal−organic chemical-vapor deposition (MOCVD) onto photoactive planar Si substrates. This tandem, vertical-wire-array-on-planar absorber was then coated by atomic layer deposition (ALD) of an amorphous TiO_2 (a-TiO_2) stabilization layer, followed by deposition of a NiO_x electrocatalyst layer. The tandem planar Si/nanowire GaAs/a-TiO_2/NiO_x photoanodes exhibited continuous solar-driven water oxidation in 1.0 M KOH(aq) for over 600 h without substantial photocurrent decay. The preservation of the nanowire morphology and structural integrity during >600 h of photoanodic operation confirms the benefits of mitigating and isolating nanoscale defects via the architecture of discretized absorbers on a self-passivating and insulating substrate. Nanoscale morphology and compositions of the photoanode after 600 h of testing were characterized to reveal the self-limiting corrosion behavior. It provides a promising approach to develop efficient but otherwise unstable absorbers such as III−V materials into defect-tolerant, corrosion-resistant photoanodes.

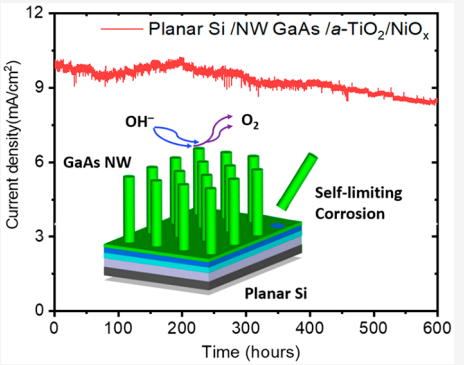

Group III-arsenic or III-phosphorus semiconductors have long-served as photoabsorbers for solar energy conversion, mainly due to broadly tunable spectral absorption, high quantum efficiency, and ease of integration with a host of dissimilar Group III−V and Group IV materials.[1−3] Recent advances in the rapid synthesis of III−V materials provide a basis for their cost-effective manufacturing.[4] However, the use of III−Vs and other corrosion-susceptible materials for photoelectrochemical reactions, including both photoanodic reactions and photocathodic reactions, is still limited, because all ranges of their compositions are predicted to undergo active dissolution in aqueous acidic or alkaline media, where efficient, membrane-bound photoelectrochemical devices can be constructed for chemical production.[5−7] Even when stabilized with 100 nm thick amorphous TiO_2 (a-TiO_2) coatings, planar III−V photoanodes for water splitting generally fail after <100 h of operation.[8]

The predominant failure mode for a-TiO_2-stabilized III−V photoelectrodes is pitting corrosion at microscopic defects that result from extrinsic imperfections or metastable phases in the protective coating.[9−11] During defect propagation, the underlying photoabsorber corrodes continuously, and the defective region propagates laterally, undercutting the coating.[12] Eventually, this process leads to the complete dissolution of the absorber material, resulting in catastrophic failure of the photoelectrode.[13] In principle, spatial isolation of defective regions and restriction of defect propagation should mitigate this mode of degradation, assuming that a sporadic and finite number of defects emerge during photoelectrode preparation or operation. As illustrated in Figure 1, an array of nanowires that are grown on a substrate that forms passivating or electrically insulating oxides upon photocorrosion or embedded in a flexible polymeric membrane can in principle provide the desired defect resistance.[14] A conceptual design advantage for such a system is that even though a defect in the stabilization coating might initiate photocorrosion, only an individual wire would corrode and dissolve locally, and the defective region would not be able to propagate to neighboring nanowires in the array.

Received: December 3, 2020
Accepted: December 9, 2020

https://dx.doi.org/10.1021/acsenergylett.0c02521
ACS Energy Lett. 2021, 6, 193−200

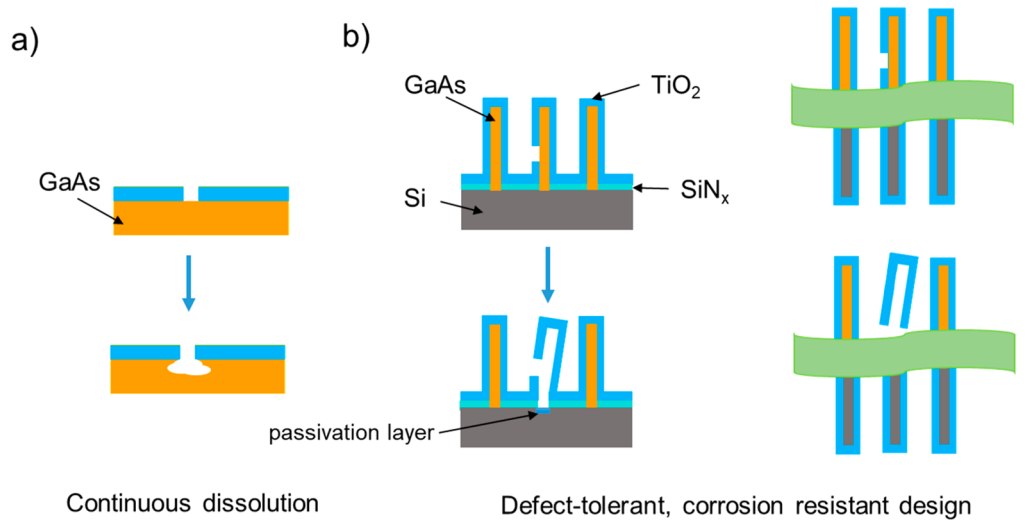

Figure 1. Schematics of (a) continuous corrosion and dissolution for failure of *a*-TiO_2-protected planar GaAs photoanodes and (b) defect-tolerant and corrosion self-limiting behavior for *a*-TiO_2-protected nanowires on a passivating or electrically insulating substrate or in a wire-embedded polymer-membrane configuration, to achieve continuous photoanodic operation.

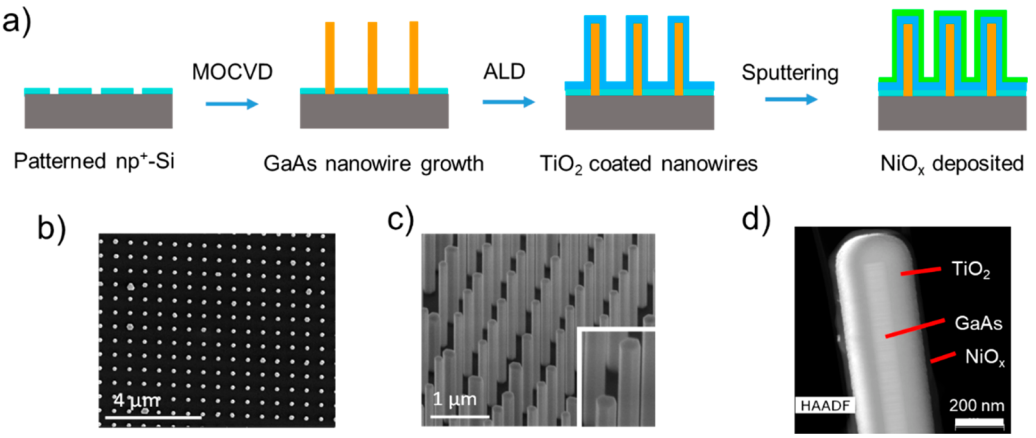

Figure 2. (a) Schematics of selective-area growth of GaAs nanowires on np^+-Si substrates and subsequent protection and catalyst integration for the as-grown GaAs nanowires for water-oxidation photoanodes. SEM micrographs of (b) the as-grown planar Si/NW GaAs/*a*-TiO_2/NiO_x, and (c) 45° from plan-view image of the same electrode region as (b). (d) TEM HAADF image of an individual nanowire.

In addition to this corrosion-mitigating strategy, photoelectrochemical (PEC) solar fuel generation, including solar-driven water splitting, CO_2 reduction, and N_2 reduction, requires a tandem architecture that incorporates at least two photoabsorbers: one for reductive fuel production and one for water oxidation, which need to operate stably to sustain fuel production.[15,16] For water splitting in particular, the bandgaps of 0.7−1.2 and 1.5−1.9 eV are required to achieve solar-to-hydrogen energy conversion efficiencies of >20%.[17,18] This design motivates the use of a tandem, monolithically integrated motif of discrete but otherwise corroding absorbers, such as III−V semiconductor wires, which are grown on a bottom absorber, such as Si. The nanowire geometry also offers opportunities to relax the strain induced by lattice mismatch, due to the high surface-area-to-volume ratio of nanowires.[19−21]

Herein, tandem planar Si/nanowire GaAs absorbers, stabilized by ∼100 nm of *a*-TiO_2 coatings, were fabricated and characterized for photoelectrochemical O_2 evolution in pH = 14 KOH(aq). This tandem structure is chosen over the polymeric membrane-bound structure, because the substrate is fixed and rigid. It is straightforward to identify and compare the same region for before and after the test. The GaAs NW/Si planar tandem structure shares the same discrete structure as the GaAs wire on Si wire tandem, which is expected for the same defect-tolerant behavior.

The (111)Si was reported to be stable for operating in an alkaline condition due the local self-passivation.[22] The stability of the GaAs nanowire top/Si bottom tandem structure was also compared directly to the behavior of GaAs nanowires grown on corrosion-susceptible substrates, e.g., degenerately doped GaAs (111)B. The comparison should test the defect-tolerant strategy and demonstrate self-limiting corrosion mitigation. Because CO_2 reduction and N_2 reduction requires light-excited electrons of high potential energy, pairing the GaAs/Si tandem photoanode with a photocathode consisting of another absorber of 1.6−2.4 eV bandgaps is efficient for liquid solar fuel production.[23,24] Furthermore, enhanced light−matter interactions, including broadband and broad-angle absorption,[25,26] have been observed for arrays of either randomly or uniformly spaced, vertically aligned nano- or microwires.

Figure 2a shows the fabrication process for TiO_2-stabilized GaAs nanowire-array photoanodes schematically. The SiN_x overlayer was first spin-coated on the np^+ Si (111) substrates

https://dx.doi.org/10.1021/acsenergylett.0c02521
ACS Energy Lett. 2021, 6, 193−200

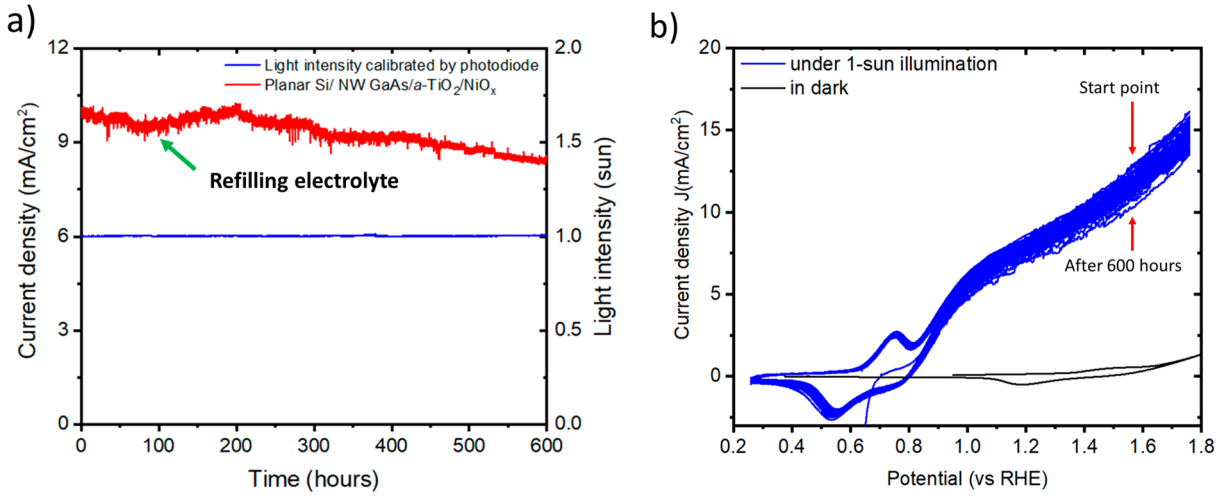

Figure 3. Continuous operation (600 h) for tandem planar Si/NW GaAs/a-TiO_2/NiO_x photoanodes in 1 M KOH: (a) Time dependence of the anodic water-oxidation current density (red), held at 1.50 V vs RHE (0.60 V vs Hg/HgO), overlaid with the light intensity as a function of time (blue); (b) light cyclic voltammetry data taken every 50 h during the stability test (blue) and dark CV data after 600 h of operation (black). The scan rate was kept at 20 mV s^{-1} for all J−E measurements.

and then etched by using e-beam lithography and reactive ion etching to form desired patterns.[25,27] Square arrays of n-type GaAs nanowires were laterally grown by metal−organic chemical-vapor deposition (MOCVD) directly on np^+-Si (111) substrates. A p^+-Si top layer was formed at the Si surface, because n^+-GaAs/p^+-Si conductive junctions exhibit low charge-conduction resistance.[28] The low resistance was also supported by device simulations (see Figure S1 and the related discussions in the Supporting Information, section S2.1). As-grown arrays of GaAs nanowires were then stabilized with atomic layer deposition (ALD)-grown a-TiO_2 coatings, followed by the deposition of a nickel oxide (NiO_x) film that served as the oxygen-evolution catalyst.[29] The same fabrication processes were also applied to an n^+-GaAs (111)B substrate as the control experiment for the evaluation of the nanowires' optoelectronic properties.

Figure 2b shows plan-view scanning-electron microscopy (SEM) images of GaAs nanowire arrays that were hetero-epitaxially grown on (111)-oriented Si substrates. A 30 min growth process produced 1.5 μm long nanowires. The growth fidelity over large areas was comparable to that observed for the GaAs nanowires grown epitaxially without a lattice mismatch on n^+-GaAs(111)B substrates.[28] The GaAs nanowires grown on either Si or GaAs substrates were ∼150 nm in diameter, and the pitch of the square-array layout was 600 nm, defined by e-beam lithography.

ALD produced individually coated, smooth sidewalls with no visible defects at the nanowire bases (Figure 2c). An inspection of individual nanowires indicated that both ∼100 nm TiO_2 and ∼10 nm NiO_x were reasonably uniform by comparing the tops and bottoms, respectively, of the coated nanowires (Figure 2d). Figure S2 illustrates the structure and layer components for the planar Si/nanowire GaAs/a-TiO_2/NiO_x photoanode, whereas Table S1 lists the layer structures for all the electrodes evaluated in this study.

The back contact of a planar Si/nanowire GaAs/a-TiO_2/NiO_x photoanode was poised at a constant potential of 1.50 versus RHE (0.60 V versus Hg/HgO) under simulated air mass (AM) 1.5G 1 sun illumination. This condition was chosen to keep consistent with the previous study.[11] The maximum work point is estimated to be ∼1.25 V vs RHE, where the current density is 8.3 mA cm^{-2}, as extrapolated quantitatively by a Matlab interpolation code. For photoandoes, high anodic potential exerts harsher conditions—unlike photocathodes where more negative potentials may serve for "protection" at cathodic potentials. The stability and performance of the photoanodes were evaluated in a three-electrode cell configuration (illustrated in Figure S3). Figure 3a shows that the photo current density decayed by <12% after 600 h of continuous operation in 1.0 M KOH(aq) under 1 sun of illumination. The total charge passed during the process is estimated to be 2.16 × 10^4 coulombs·cm^{-2}. Assuming three charges are needed to corrode per Ga or As atoms, only 0.30 coulombs·cm^{-2} of charges passed would have been required to dissolve the GaAs nanowire array fully. The photocurrent density vs potential (J−E) behavior was measured at every 50 h interval throughout 600 h of continuous operation under illumination. The overlaying J−E characteristics (Figure 3b) confirmed the high stability of the J−E performance throughout this 600 h duration. Three photoanodes of the same structure and composition were tested, and all showed comparable stability (Figure S14 and related discussion in section S2.7). From the J−E curves, we observed that at 1.25 V vs RHE, i.e., the maximum power point, the current dropped from the initial value of 8.3 to 7.5 mA cm^{-2} after 600 h, where the loss was about 9% of its initial value. This trend is consistent with the observation from the stability test.

The photoanode surface morphology was monitored over time. Figure 4a,c presents the plan-view surface morphology survey for the same photoanode before and after, respectively, continuous water oxidation for 600 h. The SEM images indicated that the macroscopic morphology remained intact after 600 h of continuous photoanodic operation in pH 14 aqueous solution. Figure 4b,d shows a magnified view for the same electrode region before and after the stability test, respectively. A comparison of the two images indicates the integrity of the nanowire array after electrochemical operation, because most features were preserved with the changes marked by red circles. Three regions for nanowire counting and calculations are randomly selected and marked by yellow rectangles in Figure 4b,d, with statistics listed in Table S2. On average, the nanowire (NW) density after the stability test was

https://dx.doi.org/10.1021/acsenergylett.0c02521
ACS Energy Lett. 2021, 6, 193−200

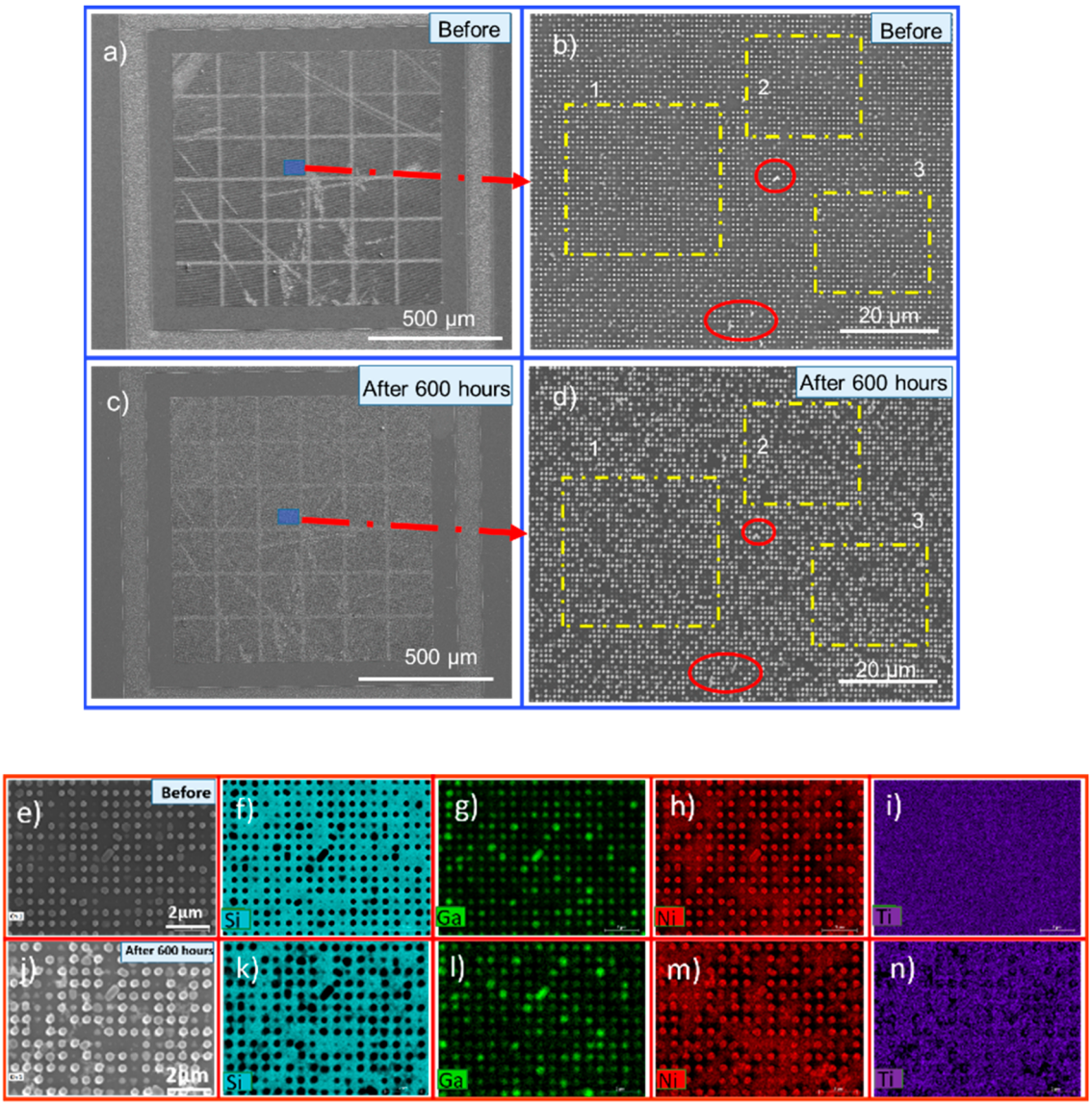

Figure 4. SEM and EDS images of the planar Si/NW GaAs/*a*-TiO_2/NiO_x photoelectrode surface. (a,c) Plan-view morphology of a planar Si/NW GaAs/*a*-TiO_2/NiO_x photoanode before and after 600 h of continuous operation under illumination, respectively; (b,d) magnified micrographs of the same selected area as marked by the small blue rectangular regions in (a,c), respectively. (e) and (j) represent one selected area on the electrode before and after the 600 h photoanodic water oxidation, respectively; (f−i) EDS elemental mapping of Si, Ga, Ni, and Ti elements for the selected area before the 600 h test; (k−n) EDS elemental mapping of Si, Ga, Ni, and Ti for the selected area after the 600 h test.

>95% of its original value. The decrease in nanowire density was consistent with the reduction of photocurrent density, i.e., a decrease of ∼1.2 ± 0.1 mA cm^{-2} based on an initial photocurrent density of 9.8 mA cm^{-2}. The 10% loss in current when less than 5% of the nanowires were lost may originate from current loss in the intact wires and/or from a decrease in light scattering and optical absorption due to loss of sporadic nanowires.[25,27] Also, the bubble attachment/detachment and the subsequent change of local pH at the electrode surface could also affect the photocurrent loss.

To evaluate whether the GaAs nanowires were intact inside the coating shell and to detect other possible structural and compositional changes after the 600 h stability test, a representative region of the photoanode was investigated by energy-dispersive X-ray spectroscopy (EDS) elemental mapping. The EDS characterizations before and after the 600 h of stability testing (fiducial marks were used to locate the same region) are shown in Figure 4e−i and j−n, respectively. The Ga EDS signal maps were compared in Figure 4g,l. The negligible changes indicated that the GaAs photoabsorbers inside the coating were well preserved throughout the 600 h of stability testing. The variation of Ga signal observed from the EDS map may originate from the variance in GaAs NW dimensions and the nature of GaAs heteroepitaxial growth on Si. Similarly, a comparison of the Ni signal in Figure 4h and m indicted that the NiO_x catalyst layer was stable during the 600 h test. The nanowire pattern according to the Ni EDS map indicated that the NiO_x film is conformal but not perfectly uniform in thickness. Moreover, by comparing Figure 4f and k, the Si signal distribution on the Si substrate was also intact, indicating minimal dissolution. After the stability test, the image contrast (Figure 4j) appears to be brighter, possibly due to changes in the nanowire surface conductivity as a result of catalytic activation of the NiO_x layer. The oxygen EDS signals

https://dx.doi.org/10.1021/acsenergylett.0c02521
ACS Energy Lett. 2021, 6, 193−200

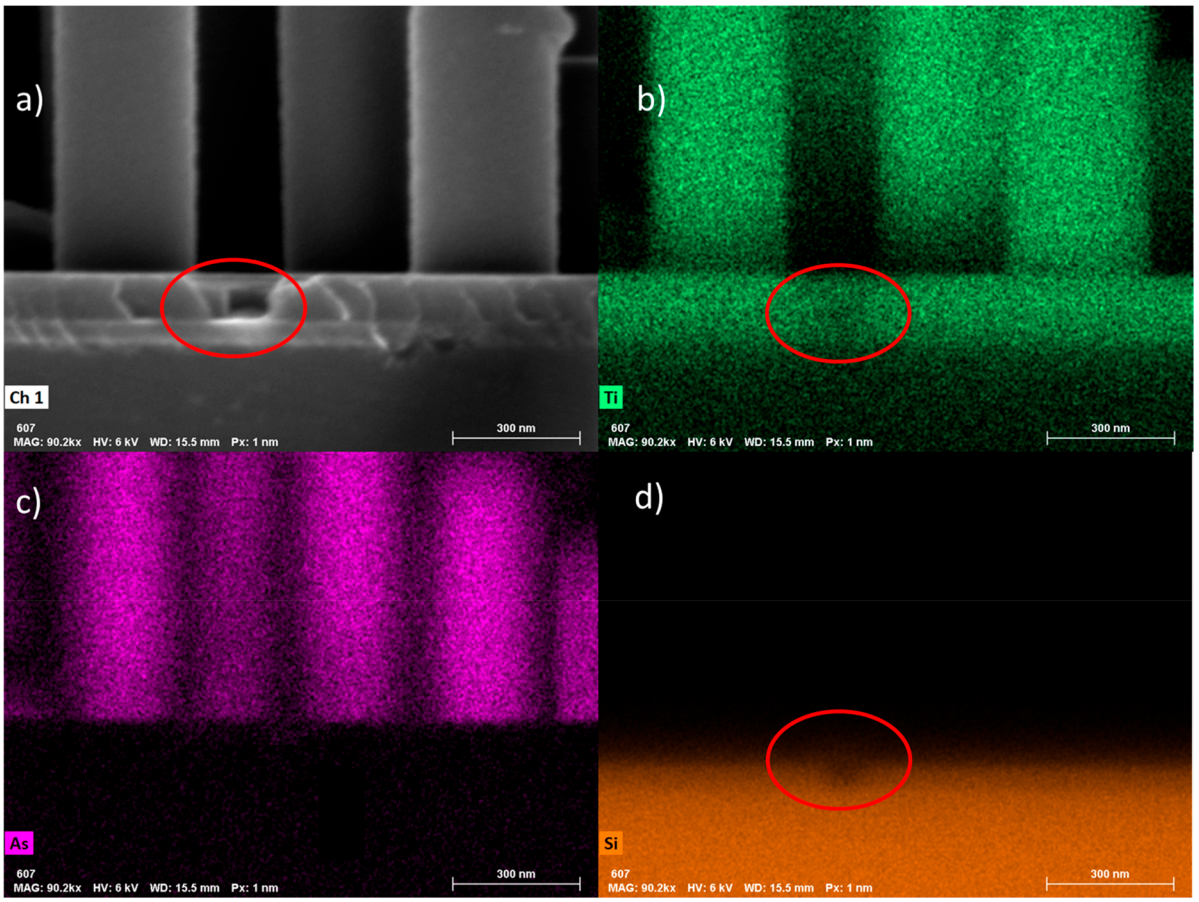

Figure 5. SEM of a defective area (marked by the red circle) on the planar Si/GaAs NW/TiO_2/NiO_x electrode. (a) The cross-sectional image; (b−d) elemental mapping for Ti, As, and Si of the region shown in (a).

were also taken, but their signals were distributed homogeneously for both before and after the test, because oxygen in various structures contributes to the EDS. No half-corroded nanowires in KOH(aq) could be found for TEM characterization, which supports the proposed corrosion mechanism, because only tens of seconds are sufficient for any exposed nanowire to be fully corroded under 1 sun of illumination.

The correlation between the nanowire-array morphology and photocurrent density validates the expected long-term stability of the planar Si/NW GaAs tandem photoanodes. By comparing Figure 4n with i (after the stability test), a signal loss for Ti was occasionally observed at locations where some nanowires had been grown initially. This behavior is consistent with the existence of defects before stability testing and/or with the emergence of defects during stability testing. Such defects that infested those failed nanowires led to their subsequent corrosion and dissolution. The local loss of the *a*-TiO_2 coatings and the Ti signal loss is consistent with an "explosive" peel-off process for the failed wires during photocorrosion: the corrosion process could be too rapid to leave any remnant *a*-TiO_2. The local loss of *a*-TiO_2 indicated that the combination of *a*-TiO_2 coatings and Si substrates effectively isolated and/or contained the corrosion defects. Sections S2.5 and S2.6 in the SI compare the stability of planar n-GaAs/*a*-TiO_2/NiO_x, planar GaAs/NW GaAs/*a*-TiO_2/NiO_x photoanodes, and those photoanodes with *a*-TiO_2 coatings as thin as 5 nm. The impermeable coatings (>5 nm thickness) combined with the self-passivating effect of Si substrates allowed the photoelectrode to tolerate the defects and contain the otherwise propagating corrosion. After the 600 h stability test, the diameters of white spots increased visually by SEM imaging. This behavior is consistent with solid NiO_x transforming into porous NiO_x/NiOOH composites, in accord with the prominent, increasing amplitude of the $Ni(OH)_2$/NiOOH redox peaks observed in the cyclic voltammetry (Figure 3b).[30] Attachment of potassium salts to the NiO_x surface (see Figure S11 potassium EDS) may also contribute to the apparent thickening of nanowire diameters. The photoanode was rinsed in water thoroughly, but some salt gels were not completely removed. Such diameter expansion obscures the Si EDS signals, making the substrate signals harder to detect. Therefore, the size of GaAs nanowire dark spots characterized by the Si elemental mapping (Figure 4f,k) seemed to grow larger.

For the 600 h TiO_2-coated planar Si/GaAs NW photoanode, we located a defective region where a nanowire was lifted off during the stability test, and then, SEM and EDS were used to characterize its cross section morphology and compositions after 600 h. From the cross section SEM (Figure 5a), we saw a defective site as marked in a red circle. No remaining GaAs signal can be detected at this defective site (Figure 5c), while in the nondefective regions, the GaAs NWs remained intact. A region of weaker Ti signal was observed from the Ti mapping image (Figure 5b), confirming the coating became permeable or opened up a pinhole at this region. In contrast, the Si elemental mapping image (Figure 5d) indicated that the Si substrate immediately surrounding the defect did not show apparent corrosion or etching. The notch observed in the Si

https://dx.doi.org/10.1021/acsenergylett.0c02521
ACS Energy Lett. 2021, 6, 193−200

EDS indicated the local corrosion and self-passivation of Si, where the nanoscale exposed Si site corroded exceptionally slowly. This observation serves as direct evidence for our hypothesis in Figure 1b. In addition, we occasionally observed an empty TiO_2/NiO_x shell on the photoanode (Figure S4), which also supported our hypothesis. One possible explanation is that the exceptionally slow corrosion rate of the nanoscale SiO_2 passivation layer was attributed to its slow ion diffusion rate. This phenomenon may be due to the compressive stress to the self-passivated SiO_2 or the densified SiO_2 confined by nanoscale openings.[31]

The $J-E$ behavior of the planar Si/NW GaAs/a-TiO_2/NiO_x photoanode was measured in 1.0 M KOH(aq) under two light intensities of simulated AM (air mass) 1.5G illumination. In addition to 1 sun of illumination (Figure 3b), Figure S5 shows the measured photoanode performance at ∼1.7 sun intensity (red curve) as well as in the absence of illumination (green curve). The photoanodic onset potential was 0.91 V vs RHE under both intensities, and the photocurrent density increased proportionally to the increase in the illumination intensity. Under 1.7 suns of illumination, the tandem planar Si/NW GaAs photoelectrode produced a light-limited photocurrent density of J_{ph} = 15.4 ± 0.2 mA cm^{-2} and an open-circuit potential of E_{oc} = 0.45 ± 0.05 V versus RHE, corresponding to a photovoltage of 0.78 ± 0.05 V relative to $E^{\circ\prime}(O_2/H_2O)$, i.e., water-oxidation potential. At $E^{\circ\prime}(O_2/H_2O)$ (1.23 V vs RHE), the current density was 12.7 mA cm^{-2}. The linear scaling relationship between the photocurrent density and local light intensity for the top GaAs nanowire absorber (Figure S6a) indicates that this wire-array architecture with high sidewall surface areas can operate favorably under mild optical concentration.[32,33] Also, the planar Si/NW GaAs/TiO_2/NiO_x photoanode exhibited nearly 100% Faradaic efficiency for quantitative O_2 production under 1 sun of illumination (oxygen generation data shown in Figure S7b).

External quantum yield data (Figure S7a) showed the current matching of the two photoabsorbers. A photocurrent density of 20 mA cm^{-2} is expected theoretically for this tandem combination of absorbers under 100 mW cm^{-2} of AM 1.5 illumination. The external quantum yield data are consistent with the optical absorption expected from a relatively sparse GaAs nanowire array at normal incidence in the absence of optimal light management methods such as the deliberate introduction of optical scatterers[34] or formation of shaped tips such as a nanocone array.[35,36] Furthermore, at such milliampere current levels, the n^+-GaAs seed layer grown on the p^+-Si top layer of the bottom np^+-Si substrate established a low-resistance ohmic contact between the top and bottom absorbers (see Supplementary Discussions for the n^+-GaAs/p^+-Si tunnel junction). Photovoltages of 0.53 and 0.23 V were obtained from the bottom Si absorber and the top GaAs absorber, respectively (Figures S8 and S6b), so the photovoltage of the planar Si/NW GaAs tandem was the addition of the photovoltage produced by the bottom Si absorber and the top GaAs absorber. Hence, photovoltage addition was achieved by direct growth of n^+-GaAs on p^+-Si to construct tandem Si/GaAs absorbers. This analysis further verifies the formation of a dual-junction GaAs nanowire/Si planar photovoltaic absorber, as reported previously.[28] The observation of a sustained 0.78 V photovoltage throughout the 600 h of continuous operation implies that the top GaAs absorber limited the performance of the device.

Even though the performance of the tandem planar Si/nanowire GaAs/a-TiO_2/NiO_x photoanodes has not yet been optimized for water splitting, it can be used for water oxidation during CO_2 reduction and N_2 reduction.[24] The performance optimization was not fully explored in this work, since the main focus is to demonstrate the defect-tolerant design. Further optimizations for optical absorption can be possibly made by varying the thickness of the TiO_2 coating and NiO_x layer for more light transmittance. Also, improved photovoltages can be obtained by (1) matching the energetics of coatings' charge-transport electronic states with the GaAs valence band[37] and (2) optimizing the growth and fabrication processes for the GaAs and Si materials explored herein. However, an optimized GaAs/Si tandem would not be optimal for unassisted water splitting, because the water-splitting tandem requires open-circuit voltages of >1.7 V and current matching between top and bottom absorbers.[38] Nonetheless, the top absorber of the defect-tolerant architecture can be straightforwardly extended to other III−V semiconductors of 1.7−1.9 eV bandgaps. For example, synthesis of $GaAs_xP_{1-x}$ wires on Si[4] or $In_xGa_{1-x}N$ wires on Si[39−41] ($0 < x < 1$) has been shown and promises stable solar-driven unassisted water-splitting devices. The same strategy is applicable to the fields of CO_2 reduction and N_2 reduction.

In summary, the tandem planar Si/NW array GaAs photoanodes reported herein serve as a model system for defect-tolerant design of corrosion-susceptible PEC devices. The photoanodes exhibited hundreds of hours of continuous operation under illumination and produced chemicals under mild optical concentrations. Moreover, successful voltage addition was obtained by the direct growth of GaAs nanowires on planar Si absorber substrates. This tandem design provides a pathway toward efficient extended stability PEC devices via monolithic integration of technologically important but otherwise unstable III−V light absorbers with Si bottom absorbers. In addition to MOCVD growth, hydride CVD promises scalable manufacturing for these potentially efficient yet heretofore expensive top absorbers.[42,43] The discretized absorber motif, each segment of which is in ohmic contact with substrates that self-passivate and self-terminate against local photocorrosion, such as Si, promises the extension of PEC stability beyond hundreds of hours. This corrosion-resistant strategy can be readily exploited for various efficient or earth-abundant absorbers that ought to be obtainable by the integration of tunable and optimized bandgaps of tandem absorbers.

■ ASSOCIATED CONTENT

Supporting Information

The Supporting Information is available free of charge at https://pubs.acs.org/doi/10.1021/acsenergylett.0c02521.

Experimental details about the fabrication process, performance, and stability tests, simulation for the p^+-Si/n^+-GaAs junction, schematics for the electrode structure, cell setup, and band diagram, SEM, EDS, and TEM for morphological and structural characterizations, additional performance data, repeated stability test results, and detailed corrosion behavior discussions (PDF)

https://dx.doi.org/10.1021/acsenergylett.0c02521
ACS Energy Lett. 2021, 6, 193−200

AUTHOR INFORMATION

Corresponding Authors

Shu Hu − *Department of Chemical and Environmental Engineering, School of Engineering and Applied Science, Yale University, New Haven, Connecticut 06520, United States; Energy Sciences Institute, West Haven, Connecticut 06516, United States;* orcid.org/0000-0002-5041-0169; Email: shu.hu@yale.edu

Nathan S. Lewis − *Division of Chemistry and Chemical Engineering, California Institute of Technology, Pasadena, California 91125, United States;* orcid.org/0000-0001-5245-0538; Email: nslewis@caltech.edu

Authors

Xin Shen − *Department of Chemical and Environmental Engineering, School of Engineering and Applied Science, Yale University, New Haven, Connecticut 06520, United States; Energy Sciences Institute, West Haven, Connecticut 06516, United States*

Maoqing Yao − *Department of Electrical Engineering, University of Southern California, Los Angeles, California 90089, United States*

Ke Sun − *Division of Chemistry and Chemical Engineering, California Institute of Technology, Pasadena, California 91125, United States*

Tianshuo Zhao − *Department of Chemical and Environmental Engineering, School of Engineering and Applied Science, Yale University, New Haven, Connecticut 06520, United States; Energy Sciences Institute, West Haven, Connecticut 06516, United States*

Yulian He − *Department of Chemical and Environmental Engineering, School of Engineering and Applied Science, Yale University, New Haven, Connecticut 06520, United States; Energy Sciences Institute, West Haven, Connecticut 06516, United States*

Chun-Yung Chi − *Department of Electrical Engineering, University of Southern California, Los Angeles, California 90089, United States*

Chongwu Zhou − *Department of Electrical Engineering, University of Southern California, Los Angeles, California 90089, United States;* orcid.org/0000-0001-8448-8450

Paul Daniel Dapkus − *Department of Electrical Engineering, University of Southern California, Los Angeles, California 90089, United States*

Complete contact information is available at: https://pubs.acs.org/10.1021/acsenergylett.0c02521

Notes

The authors declare no competing financial interest.

ACKNOWLEDGMENTS

This work was supported through the Office of Science of the U.S. Department of Energy under Award No. DE-SC0004993 to the Joint Center for Artificial Photosynthesis, a DOE Energy Innovation Hub, and under Award Number DE-SC0001013 to the Center for Energy Nanoscience, an Energy Frontier Research Center (EFRC). We thank the Materials Characterization Core at Yale West Campus for SEM characterization.

REFERENCES

(1) Khaselev, O.; Turner, J. A. A monolithic photovoltaic-photoelectrochemical device for hydrogen production via water splitting. *Science* **1998**, *280*, 425−427.

(2) Verlage, E.; Hu, S.; Liu, R.; Jones, R. J. R.; Sun, K.; Xiang, C.; Lewis, N. S.; Atwater, H. A. A monolithically integrated, intrinsically safe, 10% efficient, solar-driven water-splitting system based on active, stable earth-abundant electrocatalysts in conjunction with tandem III-V light absorbers protected by amorphous TiO_2 films. *Energy Environ. Sci.* **2015**, *8*, 3166−3172.

(3) Siddiqi, G.; Pan, Z. H.; Hu, S. III-V Semiconductor Photoelectrodes. *Semicond. Semimetals* **2017**, *97*, 81−138.

(4) Wu, J.; Li, Y. B.; Kubota, J.; Domen, K.; Aagesen, M.; Ward, T.; Sanchez, A.; Beanland, R.; Zhang, Y. Y.; Tang, M. C.; Hatch, S.; Seeds, A.; Liu, H. Y. Wafer-Scale Fabrication of Self-Catalyzed 1.7 eV GaAsP Core-Shell Nanowire Photocathode on Silicon Substrates. *Nano Lett.* **2014**, *14*, 2013−2018.

(5) Jin, J.; Walczak, K.; Singh, M. R.; Karp, C.; Lewis, N. S.; Xiang, C. X. An experimental and modeling/simulation-based evaluation of the efficiency and operational performance characteristics of an integrated, membrane-free, neutral pH solar-driven water-splitting system. *Energy Environ. Sci.* **2014**, *7*, 3371−3380.

(6) Kampmann, J.; Betzler, S.; Hajiyani, H.; Haringer, S.; Beetz, M.; Harzer, T.; Kraus, J.; Lotsch, B. V.; Scheu, C.; Pentcheva, R.; Fattakhova-Rohlfing, D.; Bein, T. How photocorrosion can trick you: a detailed study on low-bandgap Li doped CuO photocathodes for solar hydrogen production. *Nanoscale* **2020**, *12*, 7766−7775.

(7) Levy-Clement, C.; Bastide, S. Openings in photoelectrochemistry and photocorrosion of silicon. *Z. Phys. Chem.* **1999**, *212*, 123−143.

(8) Hu, S.; Lewis, N. S.; Ager, J. W.; Yang, J. H.; McKone, J. R.; Strandwitz, N. C. Thin-Film Materials for the Protection of Semiconducting Photoelectrodes in Solar-Fuel Generators. *J. Phys. Chem. C* **2015**, *119*, 24201−24228.

(9) Ros, C.; Carretero, N. M.; David, J.; Arbiol, J.; Andreu, T.; Morante, J. R. Insight into the Degradation Mechanisms of Atomic Layer Deposited TiO_2 as Photoanode Protective Layer. *ACS Appl. Mater. Interfaces* **2019**, *11*, 29725−29735.

(10) Yu, Y. H.; Sun, C. L.; Yin, X.; Li, J.; Cao, S. Y.; Zhang, C. Y.; Voyles, P. M.; Wang, X. D. Metastable Intermediates in Amorphous Titanium Oxide: A Hidden Role Leading to Ultra-Stable Photoanode Protection. *Nano Lett.* **2018**, *18*, 5335−5342.

(11) Shaner, M. R.; Hu, S.; Sun, K.; Lewis, N. S. Stabilization of Si microwire arrays for solar-driven H_2O oxidation to O_2(g) in 1.0 M KOH(aq) using conformal coatings of amorphous TiO_2. *Energy Environ. Sci.* **2015**, *8*, 203−207.

(12) Cheng, Q.; Benipal, M. K.; Liu, Q. L.; Wang, X. Y.; Crozier, P. A.; Chan, C. K.; Nemanich, R. J. Al_2O_3 and SiO_2 Atomic Layer Deposition Layers on ZnO Photoanodes and Degradation Mechanisms. *ACS Appl. Mater. Interfaces* **2017**, *9*, 16138−16147.

(13) Sun, K.; Ritzert, N. L.; John, J.; Tan, H. Y.; Hale, W. G.; Jiang, J. J.; Moreno-Hernandez, I.; Papadantonakis, K. M.; Moffat, T. P.; Brunschwig, B. S.; Lewis, N. S. Performance and failure modes of Si anodes patterned with thin-film Ni catalyst islands for water oxidation. *Sustain. Energy Fuels* **2018**, *2*, 983−998.

(14) Spurgeon, J. M.; Walter, M. G.; Zhou, J. F.; Kohl, P. A.; Lewis, N. S. Electrical conductivity, ionic conductivity, optical absorption, and gas separation properties of ionically conductive polymer membranes embedded with Si microwire arrays. *Energy Environ. Sci.* **2011**, *4*, 1772−1780.

(15) Hu, S.; Xiang, C. X.; Haussener, S.; Berger, A. D.; Lewis, N. S. An analysis of the optimal band gaps of light absorbers in integrated tandem photoelectrochemical water-splitting systems. *Energy Environ. Sci.* **2013**, *6*, 2984−2993.

(16) Singh, M. R.; Clark, E. L.; Bell, A. T. Thermodynamic and achievable efficiencies for solar-driven electrochemical reduction of carbon dioxide to transportation fuels. *Proc. Natl. Acad. Sci. U. S. A.* **2015**, *112*, E6111−E6118.

(17) Doscher, H.; Young, J. L.; Geisz, J. F.; Turner, J. A.; Deutsch, T. G. Solar-to-hydrogen efficiency: shining light on photoelectrochemical device performance. *Energy Environ. Sci.* **2016**, *9*, 74−80.

(18) Seitz, L. C.; Chen, Z. B.; Forman, A. J.; Pinaud, B. A.; Benck, J. D.; Jaramillo, T. F. Modeling Practical Performance Limits of

Photoelectrochemical Water Splitting Based on the Current State of Materials Research. *ChemSusChem* **2014**, *7*, 1372−1385.
(19) Sburlan, S.; Dapkus, P. D.; Nakano, A. Critical dimensions of highly lattice mismatched semiconductor nanowires grown in strain-releasing configurations. *Appl. Phys. Lett.* **2012**, *100*, 163108.
(20) Zhang, R.; Yang, L.; Huang, X. N.; Chen, T.; Qu, F. L.; Liu, Z.; Du, G.; Asiri, A. M.; Sun, X. P. Se doping: an effective strategy toward Fe_2O_3 nanorod arrays for greatly enhanced solar water oxidation. *J. Mater. Chem. A* **2017**, *5*, 12086−12090.
(21) Zhang, R.; Fang, Y. Y.; Chen, T.; Qu, F. L.; Liu, Z.; Du, G.; Asiri, A. M.; Gao, T.; Sun, X. P. Enhanced Photoelectrochemical Water Oxidation Performance of Fe_2O_3 Nanorods Array by S Doping. *ACS Sustainable Chem. Eng.* **2017**, *5*, 7502−7506.
(22) Yang, F.; Zhou, X. H.; Plymale, N. T.; Sun, K.; Lewis, N. S. Evaluation of sputtered nickel oxide, cobalt oxide and nickel-cobalt oxide on n-type silicon photoanodes for solar-driven O_2(g) evolution from water. *J. Mater. Chem. A* **2020**, *8*, 13955−13963.
(23) Walczak, K. A.; Segev, G.; Larson, D. M.; Beeman, J. W.; Houle, F. A.; Sharp, I. D. Hybrid Composite Coatings for Durable and Efficient Solar Hydrogen Generation under Diverse Operating Conditions. *Adv. Energy Mater.* **2017**, *7*, 1602791.
(24) Cheng, W. H.; Richter, M. H.; Sullivan, I.; Larson, D. M.; Xiang, C. X.; Brunschwig, B. S.; Atwater, H. A. CO_2 Reduction to CO with 19% Efficiency in a Solar-Driven Gas Diffusion Electrode Flow Cell under Outdoor Solar Illumination. *Acs Energy Lett.* **2020**, *5*, 470−476.
(25) Hu, S.; Chi, C. Y.; Fountaine, K. T.; Yao, M. Q.; Atwater, H. A.; Dapkus, P. D.; Lewis, N. S.; Zhou, C. W. Optical, electrical, and solar energy-conversion properties of gallium arsenide nanowire-array photoanodes. *Energy Environ. Sci.* **2013**, *6*, 1879−1890.
(26) Huang, N. F.; Lin, C. X.; Povinelli, M. L. Broadband absorption of semiconductor nanowire arrays for photovoltaic applications. *J. Opt.* **2012**, *14*, 024004.
(27) Huang, N. F.; Lin, C. X.; Povinelli, M. L. Limiting efficiencies of tandem solar cells consisting of III-V nanowire arrays on silicon. *J. Appl. Phys.* **2012**, *112*, 064321.
(28) Yao, M. Q.; Cong, S.; Arab, S.; Huang, N. F.; Povinelli, M. L.; Cronin, S. B.; Dapkus, P. D.; Zhou, C. W. Tandem Solar Cells Using GaAs Nanowires on Si: Design, Fabrication, and Observation of Voltage Addition. *Nano Lett.* **2015**, *15*, 7217−7224.
(29) Hu, S.; Shaner, M. R.; Beardslee, J. A.; Lichterman, M.; Brunschwig, B. S.; Lewis, N. S. Amorphous TiO_2 coatings stabilize Si, GaAs, and GaP photoanodes for efficient water oxidation. *Science* **2014**, *344*, 1005−1009.
(30) Oshitani, M.; Takayama, T.; Takashima, K.; Tsuji, S. A Study on the Swelling of a Sintered Nickel-Hydroxide Electrode. *J. Appl. Electrochem.* **1986**, *16*, 403−412.
(31) Hatty, V.; Kahn, H.; Heuer, A. H. Fracture toughness, fracture strength, and stress corrosion cracking of silicon dioxide thin films. *J. Microelectromech. Syst.* **2008**, *17*, 943−947.
(32) Chen, Y. K.; Xiang, C. X.; Hu, S.; Lewis, N. S. Modeling the Performance of an Integrated Photoelectrolysis System with 10 x Solar Concentrators. *J. Electrochem. Soc.* **2014**, *161*, F1101−F1110.
(33) Tembhurne, S.; Nandjou, F.; Haussener, S. A thermally synergistic photo-electrochemical hydrogen generator operating under concentrated solar irradiation. *Nat. Energy* **2019**, *4*, 399−407.
(34) Kelzenberg, M. D.; Boettcher, S. W.; Petykiewicz, J. A.; Turner-Evans, D. B.; Putnam, M. C.; Warren, E. L.; Spurgeon, J. M.; Briggs, R. M.; Lewis, N. S.; Atwater, H. A. Enhanced absorption and carrier collection in Si wire arrays for photovoltaic applications (vol 9, pg 239, 2010). *Nat. Mater.* **2010**, *9*, 368−368.
(35) Zhu, J.; Yu, Z. F.; Burkhard, G. F.; Hsu, C. M.; Connor, S. T.; Xu, Y. Q.; Wang, Q.; McGehee, M.; Fan, S. H.; Cui, Y. Optical Absorption Enhancement in Amorphous Silicon Nanowire and Nanocone Arrays. *Nano Lett.* **2009**, *9*, 279−282.
(36) Yalamanchili, S.; Emmer, H. S.; Fountaine, K. T.; Chen, C. T.; Lewis, N. S.; Atwater, H. A. Enhanced Absorption and < 1% Spectrum-and-Angle-Averaged Reflection in Tapered Microwire Arrays. *ACS Photonics* **2016**, *3*, 1854−1861.
(37) Chen, X. Y.; Shen, X.; Shen, S. H.; Reese, M. O.; Hu, S. Stable CdTe Photoanodes with Energetics Matching Those of a Coating Intermediate Band. *Acs Energy Lett.* **2020**, *5*, 1865−1871.
(38) Walter, M. G.; Warren, E. L.; McKone, J. R.; Boettcher, S. W.; Mi, Q. X.; Santori, E. A.; Lewis, N. S. Solar Water Splitting Cells. *Chem. Rev.* **2010**, *110*, 6446−6473.
(39) Fan, S. Z.; AlOtaibi, B.; Woo, S. Y.; Wang, Y. J.; Botton, G. A.; Mi, Z. T. High Efficiency Solar-to-Hydrogen Conversion on a Monolithically Integrated InGaN/GaN/Si Adaptive Tunnel Junction Photocathode. *Nano Lett.* **2015**, *15*, 2721−2726.
(40) Wang, Y. J.; Vanka, S.; Gim, J.; Wu, Y. P.; Fan, R. L.; Zhang, Y. Z.; Shi, J. W.; Shen, M. R.; Hovden, R.; Mi, Z. T. An $In_{0.42}Ga_{0.58}N$ tunnel junction nanowire photocathode monolithically integrated on a nonplanar Si wafer. *Nano Energy* **2019**, *57*, 405−413.
(41) Tournet, J.; Lee, Y.; Karuturi, S. K.; Tan, H. H.; Jagadish, C. III-V Semiconductor Materials for Solar Hydrogen Production: Status and Prospects. *Acs Energy Lett.* **2020**, *5*, 611−622.
(42) Metaferia, W.; Schulte, K. L.; Simon, J.; Johnston, S.; Ptak, A. J. Gallium arsenide solar cells grown at rates exceeding 300 μh^{-1} by hydride vapor phase epitaxy. *Nat. Commun.* **2019**, *10*, 3361.
(43) Shoji, Y.; Oshima, R.; Makita, K.; Ubukata, A.; Sugaya, T. Ultrafast growth of InGaP solar cells via hydride vapor phase epitaxy. *Appl. Phys. Express* **2019**, *12*, 052004.

https://dx.doi.org/10.1021/acsenergylett.0c02521
ACS Energy Lett. 2021, 6, 193−200